Supporting Information

Kempa et al. 10.1073/pnas.1120415109

SI Text

Materials and Methods. ***1. NW synthesis.*** Au catalysts (100 nm diameter) were dispersed on poly-L-lysine functionalized 600 nm SiO_2-on-Si wafers. Substrates were inserted into a home-built reactor and the system evacuated to a base pressure of 2.8 mTorr. Crystalline *p*-type cores were grown at 470 °C and 40 Torr for 2.5 hours with flow rates of 1, 10, and 60 standard cubic centimeters per minute (sccm) for silane (SiH_4), diborane (B_2H_6, 100 p.p.m. in H_2), and hydrogen (H_2, semiconductor grade), respectively. All shell growth over these cores was performed at 775 °C and 25 Torr. Boron-doped *p*-type shells were grown for 25–30 min with 0.15, 1.5, and 60 sccm silane, diborane, and hydrogen, respectively. Intrinsic shells were grown for 20–25 min with 0.15 and 60 sccm silane and hydrogen, respectively. Phosphorous-doped *n*-type shells were grown for 10–15 min with 0.15, 0.75, and 60 sccm silane, phosphine (PH_3, 1000 p.p.m. in H_2), and hydrogen, respectively. The calibrated shell growth rates determined from independent studies of single shell thickness vs. growth time were 1.7, 1.7, and 3 nm/ min for *p*, *i* and *n*, respectively. Following NW growth, a 30–40 nm conformal layer of SiO_2 was deposited using plasma enhanced chemical vapor deposition (PECVD) over the as-grown core/shell NWs.

2. NW shell synthesis on Au-catalyst-free NW cores. Crystalline *p*-type NW cores were grown using the same core growth protocol as above. To remove the Au-catalyst following this low-temperature NW growth and prior to higher temperature shell growth, the NW cores were removed from the reactor and immersed in KI/I_2 solution for 2 min, rinsed in deionized water, then etched in buffered hydrofluoric acid (BHF) for 1 min, and rinsed once more in deionized water. Scanning electron microscopy (SEM) analysis of NWs etched by KI/I_2 demonstrated that the Au-catalyst was removed from the NW ends as reported previously for Ge NWs (S1). Following the last water rinse, the NW growth substrate was immersed in liquid N_2 and then placed under vacuum to remove residual water without aggregation of NWs by capillary action. Intrinsic, *n*-type and SiO_2 shells were then grown as described above.

3. Al-catalyzed NW synthesis. A 10 nm thick Al film was deposited by thermal evaporation ($<1.0 \times 10^{-7}$ Torr) onto a *n*-type $\langle 111 \rangle$ Si growth substrate, the substrate was inserted into the reactor, and the system was evacuated to a base pressure of 2.8 mTorr. The substrate was annealed for 1 min at 540 °C, the temperature was reduced to 510 °C, and 3 sccm of disilane (Si_2H_6) and 97 sccm of hydrogen were introduced with a total reactor pressure of 100 Torr. After 1 min, the temperature was reduced to 475 °C and growth proceeded for 15 min. Following NW core growth, the substrate was removed from the reactor, etched for 1 min in Al etchant (Transene) at 40 °C, etched 2 min in BHF, and then dried as described above for Au-etched NWs. The NW cores were annealed for 20 min under vacuum at 775 °C and then *p*-type, intrinsic, *n*-type and SiO_2 shells were grown as described above.

4. TEM and EDS sample preparation and characterization. Ultrathin NW cross-sections for TEM investigations were prepared by embedding as-grown core/shell NWs in epoxy (Epo-Tek 353ND, Epoxy Technology) followed by degassing to remove air bubbles and overnight curing at 30 °C in a vacuum oven. Approximately 40–60 nm thick samples were sectioned (Ultra Microtome, Leica) from the cured epoxy slugs using a diamond knife (Ultra 35°, DiATOME) and transferred to lacey carbon grids for aberration corrected TEM analysis (cs-TEM, Libra 200–80 MC, Carl Zeiss NTS). For phosphorous dopant mapping by EDS, *p*/pin NWs were synthesized as described above with elevated phophorous doping in the *n*-shell (0.15, 7.5, and 60 sccm flow rates for silane, phosphine, and hydrogen, respectively). This strategy was necessary to increase signal-to-noise and to study the degree of dopant localization but not absolute concentration (approximately 1×10^{20} cm^{-3}). The aberration corrected scanning TEM (cs-STEM, Libra 200 MC, Carl Zeiss NTS) used for acquisition of EDS elemental maps is equipped with twin EDS detectors and drift correction. The EDS spectra and EDS elemental map for P are shown in Fig. S2. Maps were stored at 1024×800 resolution and acquired over 5 hours using a 400 ms pixel dwell time and 1.2 nm spot size. The P and O profiles plotted in Fig. 1*E* were obtained by averaging 200 line scans across the P and O EDS maps associated with the boxed region of the inset STEM image. The P and O line profiles also reflect a running average of ± 10 points.

5. NW device fabrication. NWs were shear transferred from growth substrates to Si_3N_4 or quartz device chips (S2). 500 nm of SU-8 2000.5 was spin-coated on the device substrate, prebaked (95 °C), and photolithography or electron beam lithography (EBL) was performed to define SU-8 etch masks on the NW shells. The SU-8 was subsequently developed and cured at 180 °C for 10 min. Following a 20 s BHF etch to remove the SiO_2 outer shell, the NWs were etched for 10–18 s in potassium hydroxide (KOH 38 vol.% in water) at 60 °C. Last, EBL followed by thermal evaporation of 4 nm of Ti and 350 nm of Pd yielded selective patterned contacts to the etched (*p*-type) core and unetched (*n*-type) shell. A 10 nm film of Ni, which serves as a charge dissipation layer, was deposited over resists for EBL fabrication on quartz substrates.

6. Device measurements. A standard solar simulator (150 W, Newport Oriel) with AM 1.5 G filter and calibrated 1-sun intensity was used in conjunction with a probe station (TTP-4, Desert Cryogenics) and semiconductor parameter analyzer (4156 C, Agilent Technologies) to obtain all device transport characteristics. Wavelength dependent photocurrent spectra were obtained with a home-built optical setup utilizing the solar simulator with AM 1.5 G filter as illumination source and a spectrometer (SpectraPro 300i, Acton Research) with 1200 g/mm grating and blaze angle of 500 nm. An uncoated Glan-Thompson calcite polarizer (10GT04, Newport) and power meter with low power Si photodetector (1918-C and 918D-UV-OD3, Newport) were used to obtain polarization-resolved absolute external quantum efficiency (EQE) spectra. The illumination power was measured from 300 to 900 nm in 5 nm increments through 1.0, 1.3, and 2.0 mm diameter circular apertures to confirm uniformity and accuracy of the power density used to calculate absolute EQE values. Device photocurrents for TE and TM polarizations were measured from 300 to 900 nm in 5 nm increments using a semiconductor parameter analyzer (4156C, Agilent Technologies). Unpolarized EQE spectra (Fig. 3) were calculated by averaging EQE data from TE and TM polarization measurements. Note that direct measurement of unpolarized spectra is not possible because of polarizing effects due to the grating and other optics used for measurement. However, the average of TE and TM spectra is equivalent to an unpolarized spectrum because unpolarized illumination is composed of two equal, orthogonal polarization states represented by TE and TM polarizations (S3). Current density and absolute EQE were calculated using photocurrent data collected as described above and the projected area of the Si NWs, which was measured by SEM (Zeiss Ultra55). In our analyses, the projected area of a NW device was taken to be the entire exposed area of the unetched NW shell when viewed normal to the plane of the substrate and does not include the area covered by 350 nm thick Ti/Pd contacts. We note that this yields an upper limit to the J_{SC} that could be achieved in a practical device.

7. FDTD calculations. For a normally incident plane wave with transverse-electric (TE) and transverse-magnetic (TM) orthogonal states, the absorption cross section of a NW or bulk Si was obtained by integrating $J \bullet E$ at each grid point, where J and E are the polarization current density and electric field, respectively. For NWs (bulk Si), the absorption cross-section (absorption efficiency) was integrated over one optical period, and the wavelength of the normally incident plane wave was scanned from 280–1000 nm with a step size of 5 nm. For NWs, the absorption efficiency was defined by the ratio of the NW absorption cross-section to the physical cross-section. EQE was calculated by multiplying the absorption efficiency by internal quantum efficiency (IQE), where IQE was assumed to be unity. The short-circuit current density (J_{SC}) at a specific wavelength was calculated as follows: $J_{SC}(\lambda) =$ EQE$\times$ (spectral irradiance of AM1.5 G spectrum at 1-sun solar intensity) $\times\lambda/1.24$. The total J_{SC} was obtained by integrating $J_{SC}(\lambda)$ over the wavelength range of 280–1000 nm. For bulk Si simulations, a spatial resolution of 5 nm was used for the *x*, *y*, and *z* directions and periodic boundary conditions were applied along the *x* and *y* directions. A perfectly matched layer was in contact with the lower *z* boundary of Si. For NWs, a spatial resolution of $5/\sqrt{3}$, 5, and 5 nm for *x*, *y*, and *z*, respectively, was used to represent the volume element for our hexagonal cross-section of a NW, where *y* lies along the NW axis and *z* lies along the propagation direction of the incident plane wave. All NW simulations included the substrates and conformal SiO_2 layer used in the experiment. Periodic boundary conditions were applied along the axis of a NW. Perfectly matched layers were applied at the other boundaries of the calculation domain. The total-field scattered-field (TFSF) method was applied to ensure that a single NW experiences an infinite plane wave. Without this method, the single NW would be simulated as a periodic array of NWs along the x-axis. To model the dispersive properties of the Si NW and Ag as a backside reflector, the Drude-critical points model was incorporated into the FDTD calculation (S4). The plasma and collision frequencies were obtained by fitting the measured refractive index and extinction coefficient of single crystal silicon (S5) and silver (S6) over the wavelength range, 280–1000 nm.

8. NW assembly. First, shear transfer (S2) was used to assemble the first level of NWs (the bottom NW in a vertical stack) onto quartz device substrates. After spin coating poly(methyl methacrylate) (PMMA) C5 over the device substrate, electron beam lithography was performed to open 0.5-μm wide trenches over selected NWs. A second layer of NWs was transferred over the patterned PMMA, followed by addition of a water droplet, which was blown across the device region using dry N_2. After this process, NWs were drawn into the trenches defined over the first level NWs to yield two vertically stacked NWs. PMMA was removed with a UV/O_3 asher at 200 °C for 10 min, and subsequent device fabrication proceeded as described above.

9. Dark saturation current. Dark current-voltage ($I - V$) measurements for each NW were fit within the linear regime to extract I_0 from the ideal diode equation, $\ln(I) = qV/(nkT) + \ln(I_0)$, where q is elementary charge, V is voltage, n is the diode ideality factor, k is the Boltzmann constant, and T is temperature.

10. Comparison of V_{OC} between planar and NW devices. We have also compared our coaxial Si NW device characteristics to those of planar Si solar cells as a means to measure their performance and potential for improvement. The direct comparison of V_{OC} discussed in the main text shows a lower value for our NW devices. We wish to assess whether higher V_{OC}'s could be obtained through further improvement of, for example, junction quality in these NW structures. Before addressing this question, we estimated the contributions to lower V_{OC} in coaxial NWs arising from differences in their geometry and their incomplete light absorption relative to planar Si solar cells.

First, and as discussed previously (S7, S8), there is a larger p-n or p-i-n junction area for devices with cylindrical versus planar geometries for a given projected area. The change in V_{OC} due to increased junction area of a cylindrical structure can be accounted for by a logarithmic dependence on γ, which relates the junction area in a NW to the junction area in a planar device with an equivalent projected area as reported (S7, S8):

$$V_{\mathrm{OC}} = (nk_{\mathrm{B}}T/q)\ln(I_{\mathrm{SC}}/\gamma I_0) \tag{S1}$$

where n is the ideality factor, k_B is the Boltzmann constant, q is charge, I_{SC} is the short-circuit current, and I_0 is the dark saturation current. We estimate γ by assuming the NWs are perfect cylinders with a junction area defined by the outside surface of the cylinder, yielding $\gamma = \pi$. Using the parameters for one of the better p/in devices ($V_{OC} = 0.475$ V; $n = 1.61$; $I_{SC} = 155$ pA; $I_0 = 1.1$ fA), we calculate a positive shift in V_{OC} of $\Delta V_{OC} = 0.044$ V and a final V_{OC} of 0.519 V.

Second, we can also account for the effect of incomplete light absorption in the coaxial Si NW devices by introducing a factor α, which relates the I_{SC} of a NW device to that of a conventional Si solar cell with complete light absorption as:

$$V_{\mathrm{OC}} = (nk_{\mathrm{B}}T/q)\ln(\alpha I_{\mathrm{SC}}/\gamma I_0). \tag{S2}$$

We estimate α by noting that the short-circuit current density (J_{SC}) of our p/in NWs is 6–7 mA/cm^2 whereas the J_{SC} of state-of-the-art bulk Si solar cells (S9) is approximately 43 mA/cm^2. Using a value of $\alpha = 7$ and $\gamma = \pi$, we arrive at $\Delta V_{OC} = 0.119$ V and a final V_{OC} of 0.594 V. The values of V_{OC} for high-quality multicrystalline and single crystal Si solar cells with complete light absorption are 0.66–0.7 V (S9). Hence, we can conclude that our measured coaxial NW V_{OC} is close to the best that might be expected (with the above corrections), although the difference of 0.07 to 0.11 V does suggest that further improvement might be achieved by additional optimization of the core/shell structures and surface passivation.

1. Woodruff JH, Ratchford JB, Goldthorpe IA, McIntyre PC, Chidsey CED (2007) Vertically oriented germanium nanowires grown from gold colloids on silicon substrates and subsequent gold removal. *Nano Lett* 7:1637–1642.
2. Javey A, Nam SW, Friedman RS, Yan H, Lieber CM (2007) Layer-by-layer assembly of nanowires for three-dimensional, multifunctional electronics. *Nano Lett* 7:773–777.
3. Hecht E (2002) *Optics* (Addison Wesley, San Francisco).
4. Vial A, Laroche T (2008) Comparison of gold and silver dispersion laws suitable for FDTD simulations. *Appl Phys B: Lasers Opt* 93:139–143.
5. Lide DR (2008) *CRC Handbook of Chemistry and Physics: A Ready-Reference Book of Chemical and Physical Data* (CRC Press, Boca Raton).
6. Johnson PB, Christy RW (1972) Optical constants of the noble metals. *Phys Rev B* 6:4370–4379.
7. Kayes BM, Atwater HA, Lewis NS (2005) Comparison of the device physics principles of planar and radial p-n junction nanorod solar cells. *J Appl Phys* 97:114302–114311.
8. Boettcher SW *et al.* (2010) Energy conversion properties of vapor-liquid-solid-grown silicon wire-array photocathodes. *Science* 327:185–187.
9. Green MA, Emery K, Hishikawa Y, Warta W (2010) Solar cell efficiency tables (version 36). *Prog Photovoltaics* 18:346–352.
10. Cao LY *et al.* (2010) Semiconductor nanowire optical antenna solar absorbers. *Nano Lett* 10:439–445.

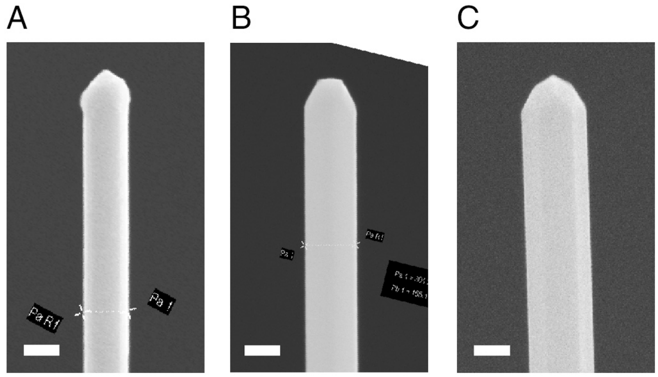

Fig. S1. SEM images of as-grown core/shell Si NWs. (*A*) p/n NW showing a smooth, faceted surface for the majority of the NW but some surface roughness toward the tip of the NW. Markings and lettering result from measurement of the NW diameter, which is approximately 265 nm; scale bar, 200 nm. (*B*) p/pn NW showing a smooth surface and faceted tip. Markings and lettering result from measurement of the NW diameter, which is approximately 300 nm; scale bar, 200 nm. (*C*) p/pin NW showing a smooth, faceted surface and faceted tip. NW diameter is approximately 360 nm; scale bar, 200 nm.

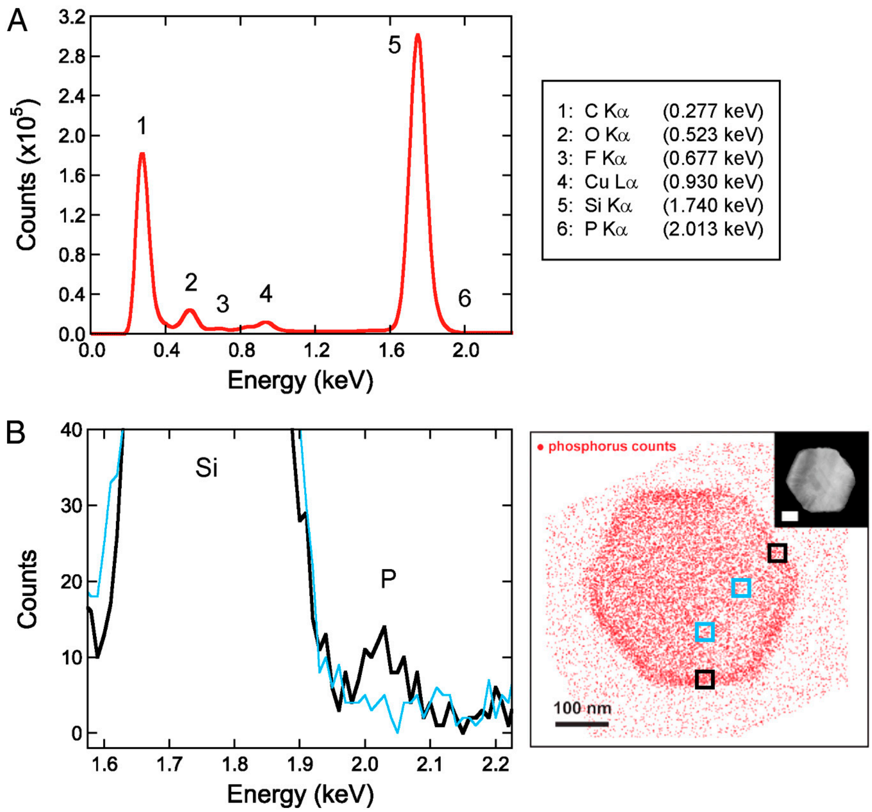

Fig. S2. EDS spectra of *p*/pin NW sections for P dopant profiling. (*A*) EDS spectrum from 0–2.2 keV after 5 h acquisition from an approximately 60-nm thick *p*/pin NW section. Peaks characteristic of specific elements are labeled and are identified in the panel at right. (*B*) EDS spectra from 1.6–2.2 keV corresponding to inner-shell (blue) and outer-shell (black) regions of the NW cross section. *Right* shows a spatial map of P X-ray counts (red), which appear in greater number and density within the outer 20–30 nm of the cross section. *Inset* displays the STEM image of the cross section; scale bar 100 nm. The inner-shell (blue) and outer-shell (black) spectra represent a sum of all X-ray counts within the two blue and two black boxed regions, respectively. The spectra demonstrate that X-ray counts from the outer-shell region give rise to a peak clearly identifiable as P and distinguishable from the background. X-ray counts from the inner region do not produce a clear P peak and are attributed to a combination of dark counts and the tail of the strong Si peak. The line profile for P in Fig. 1*E* was calculated from the same dataset, where the large apparent background signal for the central approximately 300 nm of the P line profile in Fig. 1*E* is also attributable to a combination of dark counts and the tail of the strong Si peak.

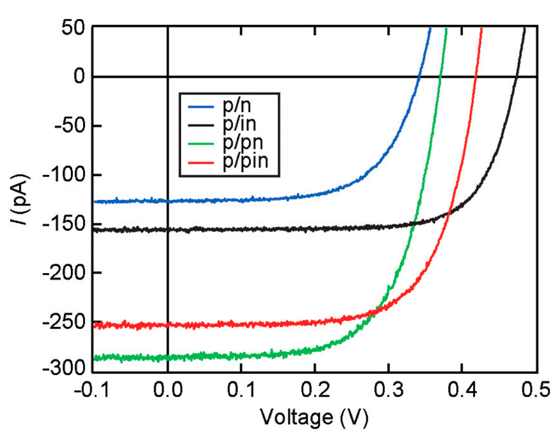

Fig. S3. Measured light $I-V$ characteristics for different NW structures. Illuminated current-voltage ($I-V$) traces for the 4 NW devices shown in Fig. 2*B*. Results show that all devices routinely exhibit I_{SC} values greater than 100 pA and that transport characteristics are recorded at high resolution to enable precise measurement of device metrics (I_{SC}, V_{OC}, FF).

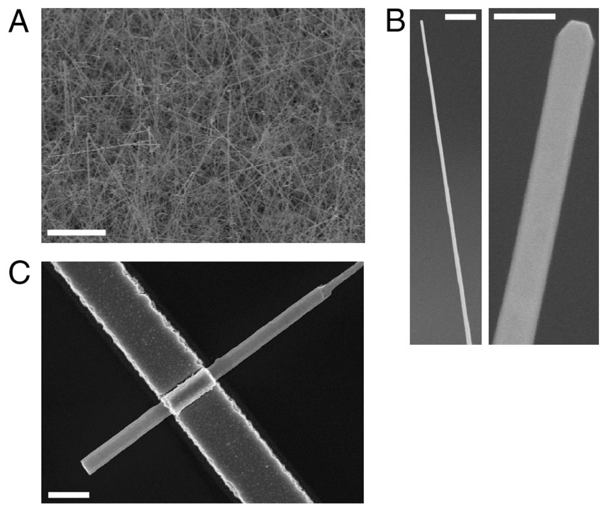

Fig. S4. Synthesis and fabrication of Al-catalyzed *i*/pin NW devices. (*A*) SEM image of Al-catalyzed intrinsic Si NW cores that are 30–50 μm long, 70–120 nm in diameter, and exhibit approximately 25 nm of radial taper over 30 μm; scale bar, 20 μm. (*B*) SEM images of coaxial NWs after growth of *p*-*i*-*n* shells on the Al-catalyzed cores. The NW surface is relatively smooth over the length of the NW (*Left*; scale bar, 2 μm) but is not as smooth and faceted as observed for Au-catalyzed core/shell NWs. Faceted surfaces were typically found within 10 μm of the NW tip (*Right*; scale bar, 200 nm). (*C*) SEM image of an Al-catalyzed *i*/pin NW solar cell ($I-V$ data for this device are plotted as the gray curve in Fig. 2*D*); scale bar, 1 μm. Comparison of the V_{OC} (I_0) metrics for Al- and Au-catalyzed *i*/pin NW devices, 0.23 V (0.8 pA) and 0.40 V (13.0 fA), respectively, highlights the substantially improved electrical quality of NWs synthesized from Au-catalyzed cores. Devices were fabricated using the same protocol as for other NWs (see *Materials and Methods*).

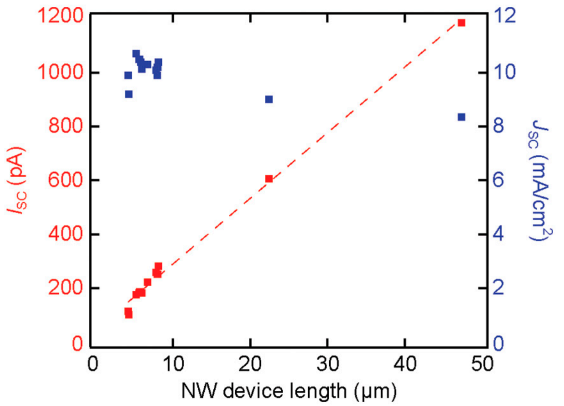

Fig. S5. Scaling of photocurrent with NW length. I_{SC} (red squares) and J_{SC} (blue squares) values for 14 *p*/pin devices plotted as functions of the exposed NW length. Results show that I_{SC} scales linearly over a range of NW lengths spanning at least one order of magnitude with values ranging from 114 pA (4.3 μm) to 1186 pA (47.3 μm). The corresponding J_{SC} values for these devices, 9.9 and 8.4 mA/cm^2, and average for all of the 14 devices, 10.0 ± 0.7 mA/cm^2 show that J_{SC} is relatively constant as expected.

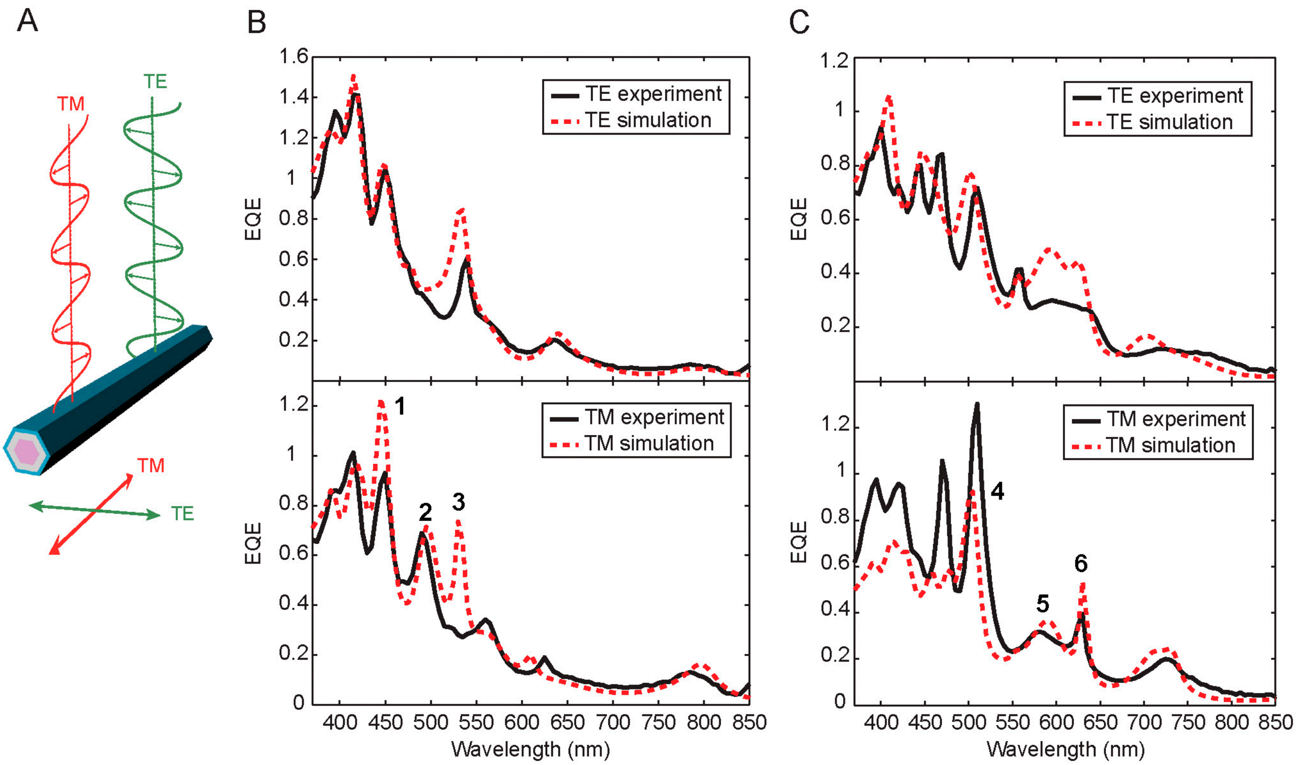

Fig. S6. External quantum efficiencies for *p*/in and *p*/pin NWs at TE and TM polarizations. (*A*) Schematic of the transverse-electric (TE) and transverse-magnetic (TM) electric field polarizations relative to the NW structure. (*B*) and (*C*) External quantum efficiency (EQE) as a function of wavelength (black curves) measured for a *p*/in NW (*B*) and *p*/pin NW (*C*) using TE (top) and TM (bottom) polarizations. Red dashed curves are FDTD simulations (see *Materials and Methods*) assuming a hexagonal shape for the NW and height of 240 nm for the *p*/in and 305 nm for the *p*/pin NW. The mode spatial profiles of peaks labeled 1–6 in the TM spectra are illustrated in Fig. 3*C* and are labeled identically in the manuscript. Peaks in the spectra correspond to absorption in the NW due to either Fabry-Perot or whispering-gallery resonant modes. These modes shift in frequency as the diameter of the NW varies. Specifically, many of the differences between the spectra of the *p*/in and *p*/pin NW can be explained by the approximately 80-nm larger diameter of the latter. In addition, the *p*/pin structure supports a larger number of resonant modes, thus explaining the large number of peaks present in the *p*/pin spectrum versus the *p*/in spectrum.

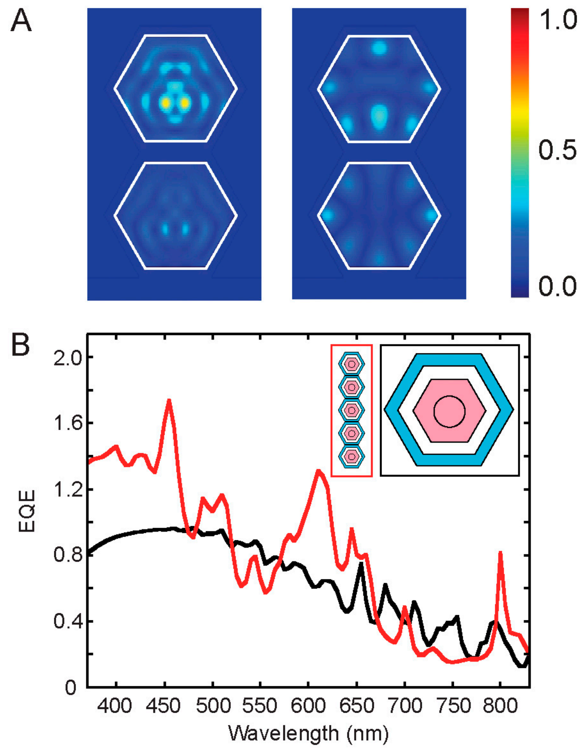

Fig. S7. NW vertical stacks. (*A*) Simulated absorption mode profiles of the double-NW stack for TE polarization at $\lambda = 425$ nm (*Left*) and for TM polarization at $\lambda = 545$ nm (*Right*). The absorption modes present in the top NW are preserved in the bottom NW, and this effect permits the broadband enhancement observed in the experimental and simulated EQE spectra for the double-NW stack (Fig. 5*A*). (*B*) Simulated EQE spectra for a 5-NW vertical stack (red curve) and a single micron-wire (black) with equivalent Si height to the 5-NW stack. *Inset*: schematic comparing a 5-NW vertical stack against a single micron-wire with Si height (1200 nm) equivalent to that of the stack. The 5-NW stack attains a maximum EQE of 1.74, which is substantially larger than the maximum of 0.97 for the single micron-wire of equal height. The EQE >1 is a manifestation of the fact that individual NWs within the stack exhibit absorption cross-sections greater than their physical cross-sections and thus absorb photons from outside of their physical projected area; this is referred to as the optical antenna effect (S10).